Smooth Crustal Velocity Models Cause a Depletion of High-Frequency Ground Motions on Soil in 2D Dynamic Rupture Simulations

Yihe Huang*[1]

ABSTRACT

A depletion of high-frequency ground motions on soil sites has been observed in recent large earthquakes and is often attributed to a nonlinear soil response. Here, I show that the reduced amplitudes of high-frequency horizontal-to-vertical spectral ratios (HVSRs) on soil can also be caused by a smooth crustal velocity model with low shear-wave velocities underneath soil sites. I calculate near-fault ground motions using both 2D dynamic rupture simulations and point-source models for both rock and soil sites. The 1D velocity models used in the simulations are derived from empirical relationships between seismic wave velocities and depths in northern California. The simulations for soil sites feature lower shear-wave velocities and thus larger Poisson's ratios at shallow depths than those for rock sites. The lower shear-wave velocities cause slower shallow rupture and smaller shallow slip, but both soil and rock simulations have similar rupture speeds and slip for the rest of the fault. However, the simulated near-fault ground motions on soil and rock sites have distinct features. Compared to ground motions on rock, horizontal ground acceleration on soil is only amplified at low frequencies, whereas vertical ground acceleration is deamplified for the whole frequency range. Thus, the HVSRs on soil exhibit a depletion of high-frequency energy. The comparison between smooth and layered velocity models demonstrates that the smoothness of the velocity model plays a critical role in the contrasting behaviors of HVSRs on soil and rock for different rupture styles and velocity profiles. The results reveal the significant role of shallow crustal velocity structure in the generation of high-frequency ground motions on soil sites.

KEY POINTS

- I use dynamic rupture models to investigate the variability of ground motions on soil and rock sites.
- Smooth velocity models with low seismic wave velocities deamplify high-frequency ground motions on soil.
- The models can better inform strong ground motion simulations and the interpretation of near-field data.

INTRODUCTION

It is well known that near-surface site effects significantly contribute to strong ground motions from earthquakes. In particular, sedimentary basins or soil sites are common in seismically active regions and are often considered to amplify ground motions due to seismic wave reverberations. However, especially for large earthquakes, the amplification of ground motions seems to strongly depend on wave frequencies. For example, in the 2019 M_w 7.1 Ridgecrest earthquake, the amplitudes of horizontal-to-vertical spectral ratios (HVSRs) at deep alluvium sites are much lower than those at thin alluvium and rock sites for frequencies higher than 3 Hz (Hough *et al.*, 2020). A similar depletion of high-frequency energy on soil sites has been shown for the 1985 M_w 8.0 Michoacan, Mexico, earthquake, the 1989 M_w 6.9 Loma Prieta, California, earthquake (Beresnev and Wen, 1996), the 1994 M_w 6.7 Northridge, California, earthquake (Field *et al.*, 1997), the 2015 M_w 7.8 Gorkha, Nepal, earthquake (Dixit *et al.*, 2015), and the 2016 M_w 5.9 southeast off-Mie, Japan, earthquake (Kubo *et al.*, 2019). Such characteristics of high-frequency ground motions are usually attributed to the nonlinear soil response associated with an increase in damping and a reduction in shear modulus for large shear strain (Beresnev and Wen, 1996). It is worth noting that low-rise buildings on soil sites may experience less

1. Department of Earth and Environmental Sciences, University of Michigan, Ann Arbor, Michigan, U.S.A., https://orcid.org/0000-0001-5270-9378 (YH)

*Corresponding author: yiheh@umich.edu

Cite this article as Huang, Y. (2021). Smooth Crustal Velocity Models Cause a Depletion of High-Frequency Ground Motions on Soil in 2D Dynamic Rupture Simulations, *Bull. Seismol. Soc. Am.* **XX**, 1–14, doi: 10.1785/0120200311

damage due to the significant reduction of high-frequency ground motions (Trifunac and Todorovska, 1998).

However, it is still unclear how properties of near-surface materials, including seismic wave velocities, Poisson's ratio, and attenuation parameters, contribute to the variability in site responses to seismic waves and whether the velocity structure underneath soil sites may cause the depletion of high-frequency energy in HVSRs. The classification of near-surface site conditions is primarily based on the time-averaged shear-wave velocity of the top 30 m of the crust (Park and Elrick, 1998), V_{S30}, which is shown to correlate with geologic units in California (Wills *et al.*, 2000) and ground-motion amplification (Field, 2000). For broad site classifications used by National Earthquake Hazards Reduction Program, rock sites should have V_{S30} larger than 760 m/s, whereas soil sites can be further classified to soft soil (site class E, $V_{S30} \le 180$ m/s), stiff soil (site class D, $180 < V_{S30} \le 360$ m/s), and very dense soil (site class C, $360 < V_{S30} \le 760$ m/s) (Building Seismic Safety Council [BSSC], 2001).

The low V_{S30} of soil sites leads to Poisson's ratios considerably larger than 0.25, the value for a perfectly isotropic elastic material, because the compressional-wave velocity (V_P) is not reduced at the same rate as the shear-wave velocity (V_S) for shallow depths. Brocher (2005) compiled V_P and V_S from borehole logs, vertical seismic profiles, laboratory measurements, and tomography studies for a variety of rocks, primarily in California. The data show that V_S varies more rapidly with V_P when V_P is less than 3.75 km/s, resulting in Poisson's ratios between 0.25 and 0.5 in the shallow crust (e.g., top 1–2 km). Especially for young, saturated sediments, the Poisson's ratio approaches 0.5 as V_S quickly drops to 100 m/s when V_P is reduced to 1500 m/s. Based on the empirical relationship between V_P and V_S (equation 9 in Brocher, 2005), soil sites with V_{S30} less than 760 m/s should have Poisson's ratios larger than 0.43. Taking into consideration large Poisson's ratios at shallow depths can help improve the stability of hypocenter determination (Nicholson and Simpson, 1985).

Another factor that can strongly affect ground motions is seismic wave attenuation of near-surface materials, quantified by the Q-values. Based on the borehole data of local earthquakes in California, Abercrombie (1997) showed that over 90% of the attenuation occurs within the upper 3 km, and the near-surface Q is very low (i.e., $Q_P \sim 26$ and $Q_S \sim 15$ in the upper 300 m). The study concluded that the near-surface attenuation has a weak dependence on site conditions, as Q is more sensitive to fracture density, temperature, and fluid content rather than rock types. Other studies (e.g., Bethmann *et al.*, 2012; Edwards and Fäh, 2013; Wang *et al.*, 2016) also found similar attenuation parameters for soil and rock sites in Europe, Middle East, and Asia. However, the 3D attenuation models of the southern California crust reveal low Q_P and Q_S values in the top 1 km layer of major sedimentary basins and high Q zones that correspond to the high-velocity rocks of the mountain ranges (Hauksson and Shearer, 2006). Van Houtte *et al.* (2011) also validated the correlation between V_{S30} and the high-frequency decay parameter κ using ground-motion data from both the Kiban–Kyoshin network (KiK-net) in Japan and the Next Generation Attenuation of Ground Motions database. Neighbors *et al.* (2015) showed that κ estimated from the 2010 Maule, Chile, aftershocks exhibits site-condition dependence, but the overlap of error bars of attenuation parameter measurements suggests the difference between hard rock and soil sites may be insignificant.

The observed low V_S, large Poisson's ratio, and possible low Q_S of soil sites encourage the hypothesis that they may partially contribute to the features of high-frequency ground motions. 3D velocity models with low V_S and large Poisson's ratios for soil sites are commonly implemented in kinematic ground-motion simulations (e.g., Olsen, 2000; Frankel *et al.*, 2009; Aagaard *et al.*, 2010; Taborda and Bielak, 2014; Asano *et al.*, 2016; Pitarka *et al.*, 2016; Rodgers *et al.*, 2018), though there is still a limitation in the lowest V_S that can be resolved. However, due to the lack of observational constraints or for computational convenience, ground-motion simulations may also assume a constant Poisson's ratio inside the sedimentary basin that is much lower than observed values (e.g., Meza-Fajardo *et al.*, 2016) or velocity models with a few layers. Some kinematic ground-motion simulations also explicitly consider the reduction of stiffness during nonlinear soil deformation by correcting site responses (e.g., Esmaeilzadeh *et al.*, 2019; Rodgers *et al.*, 2020).

Motivated by the contrasting behaviors of HVSRs on soil and rock sites in the 2019 M_w 7.1 Ridgecrest earthquake (Hough *et al.*, 2020), I characterize the contributions of shallow velocity structure to the differences of ground-motion amplitudes, frequency contents, and HVSRs on soil and rock sites by simulating 2D dynamic rupture propagating on a vertical 1D fault. Dynamic rupture simulations calculate kinematic rupture processes of earthquakes by respecting fault physics and considering the interaction between fault stress and frictional strength as well as seismic wave propagation in the surrounding medium, leading to realistic scenarios of strong ground motions (e.g., Harris *et al.*, 2018). Using dynamic rupture simulations helps differentiate the respective contributions of earthquake source and seismic wave propagation, which are both affected by the velocity structure and attenuation parameter. In the Methodology section, I discuss the velocity model, attenuation parameters, stresses, and frictional parameters used in the dynamic rupture simulations. In the Results section, I present the source characteristics of simulated rupture (e.g., slip, slip rate, and rupture speed) and compare the acceleration waveforms and HVSRs recorded on soil and rock sites. I show that a smooth velocity model combined with low V_S can give rise to diminished amplitudes of high-frequency HVSRs in soil simulations.

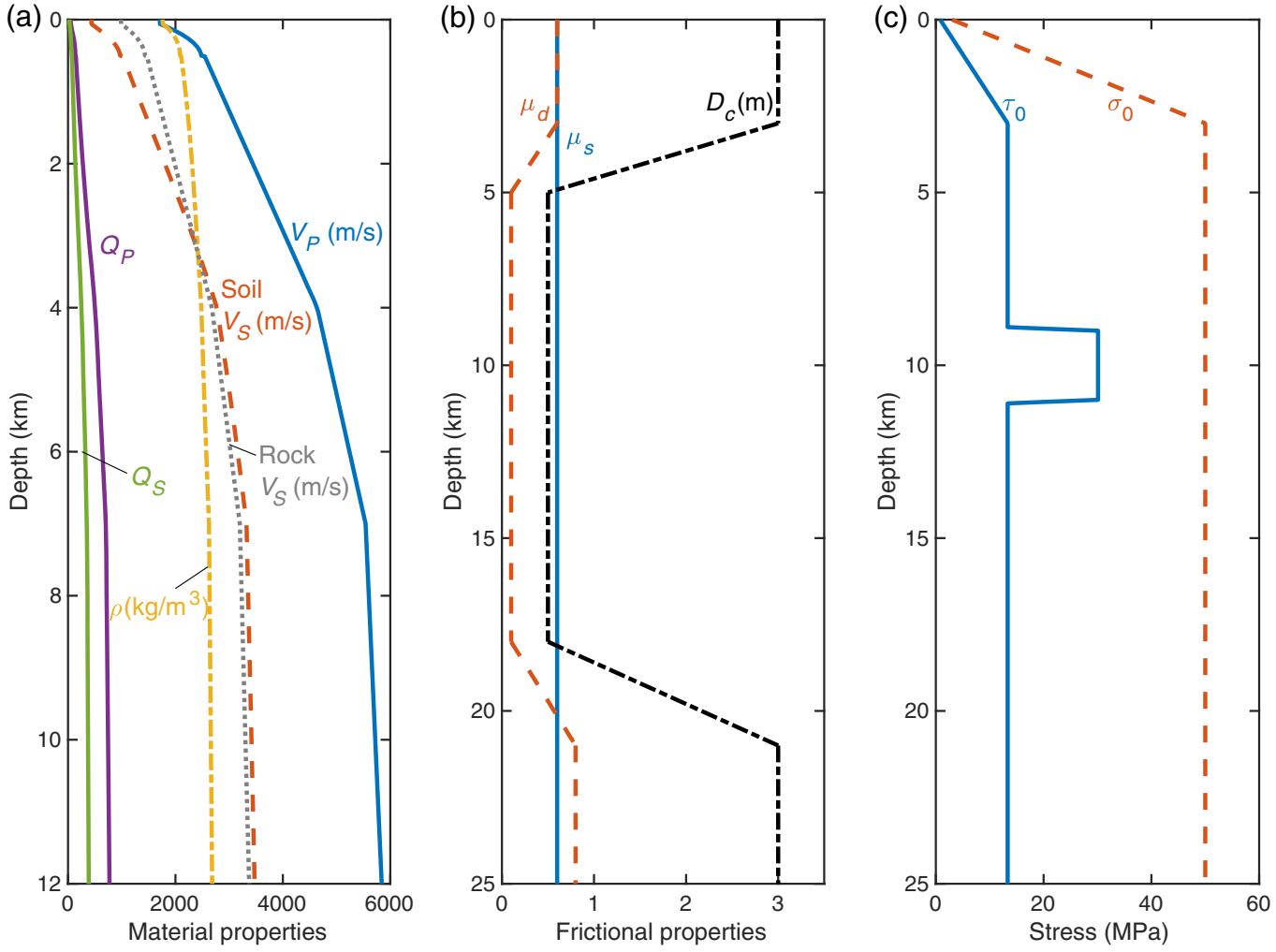

Figure 1. Depth variations of (a) material properties, (b) frictional parameters, and (c) fault stresses in model S. The dotted line in (a) shows the shear-wave velocity in model R. Model R uses the same density, compressional-wave velocity, fault friction, and stresses as shown in panels (a–c). The color version of this figure is available only in the electronic edition.

METHODOLOGY

In both 2D dynamic rupture simulations and point-source models, I use a 1D velocity model derived from empirical relationships between seismic wave velocities and depths in northern California (Brocher, 2008). Because Holocene and Plio-Quaternary deposits can greatly amplify ground motions in northern California, I adopt the depth variations of seismic wave velocities for Holocene and Plio-Quaternary sedimentary rocks at depths less than 500 m and for older Cenozoic sedimentary rocks at depths more than 500 m (Table 1; Fig. 1a). Because the maximum resolvable frequency of ground motions is determined by the slowest seismic wave velocity in the simulations, V_P and V_S in the top 60 m are kept constant and equal to the values at 60 m depth to resolve ground motions at high frequencies. The site condition is classified as a very

TABLE 1
Depth Variations of V_P and V_S for Simulated Soil Sites

Depth z (km)	V_P (km/s)	V_S (km/s)
$0 < z < 0.06$	$V_P = 1.711$	$V_S = 0.436$
$0.06 \le z < 0.5$	$V_P = 1.5 + 3.735z - 3.543z^2$	$V_S = 0.7858 - 1.2344V_P + 0.7949V_P^2 - 0.1238V_P^3 + 0.0064V_P^4$
$0.5 \le z < 4$	$V_P = 2.24 + 0.6z$	
$4 \le z < 7$	$V_P = 4.64 + 0.3(z - 4)$	
$7 \le z < 12$	$V_P = 5.54 + 0.06(z - 7)$	

dense soil given V_{S30}= 436 m/s. I refer to this velocity model as model S ("S" stands for soil) for the rest of this article. The Poisson's ratio in model S can be calculated from $\frac{(V_P/V_S)^2-2}{2(V_P/V_S)^2-2}$ using V_P and V_S in Table 1. To compare ground motions recorded at soil and rock sites, I use a different 1D velocity model based on the same V_P versus depth relationship, but with a Poisson's ratio of 0.25. Hence, $V_{S30} = 988$ m/s in this velocity model, and the site condition is classified as a rock site. I refer to this velocity model as model R ("R" stands for rock) for the rest of this article. The major difference between velocity models S and R is at depths shallower than 3 km, in which V_S is significantly lower in model S (dashed and dotted lines in Fig. 1a).

I calculate density from V_P using the Nafe–Drake curve (Ludwig *et al.*, 1970; Brocher, 2005). I estimate Q_S from V_S using the relationship ($Q_S = -16 + 104.13V_S - 25.225V_S^2 + 8.2184V_S^3$ for 0.3 km/s $< V_S <$ 5 km/s) constrained by the forward modeling of strong ground motions from the 1994 Northridge earthquake (Graves and Pitarka, 2004; Brocher, 2008). Q_P is assumed to be twice the value of Q_S (Brocher, 2008). Like seismic wave velocities, Q_P and Q_S are kept constant in the top 60 m ($Q_P = 50$ and $Q_S = 25$). I also investigate the effects of the same attenuation profiles for soil and rock simulations in the Results section, given the possible weak dependence of near-surface attenuation on site conditions (Abercrombie, 1997; Bethmann *et al.*, 2012; Edwards and Fäh, 2013; Wang *et al.*, 2016).

I simulate along-dip rupture propagation as mode II rupture on a 1D vertical fault governed by a linear slip-weakening friction law (Ida, 1972; Andrews, 1976), which describes the drop of friction coefficient from the static level μ_s to the dynamic level μ_d when slip reaches the critical slip distance, D_c (Fig. 1b). A free surface is applied to the top boundary of the modeling domain, whereas the other boundaries are absorbing boundaries (Clayton and Engquist, 1977). Synthetic waveforms are calculated on the surface at distances of 5, 10, and 15 km from the fault. The station-fault distances are chosen to be similar to those in the ground-motion analysis of the 2019 Ridgecrest earthquake (Hough *et al.*, 2020).

Frictional parameters and fault stresses vary along depth in the simulations. Both μ_d and D_c are constant at seismogenic depths (5–18 km), but increase at shallower and deeper parts to allow earthquake rupture to stop (Fig. 1b). Using $D_c = 1$ m at shallow depths does not have a significant impact on the resulting earthquake rupture and ground motions at the distances considered in this study (i.e., 5–15 km), but the choice of D_c can have a large effect on ground motions at distances closer to the fault (e.g., Wang *et al.*, 2019). Effective normal stress σ_0 increases linearly with depth for the first 3 km and remains a constant value of 50 MPa for the rest of the fault (Fig. 1c). Initial shear stress τ_0 follows the variation of effective normal stress except inside the nucleation zone to keep an S ratio of 2 ($S = \frac{\mu_s\sigma_0-\tau_0}{\tau_0-\mu_d\sigma_0}$). Dynamic rupture is nucleated at a depth of 10 km by a 2-km-long overstressed patch with the initial shear stress τ_0 0.3% higher than the static shear strength $\mu_s\sigma_0$. As rupture propagates, seismic waves are radiated into the surrounding medium, which generates ground motions.

Dynamic rupture is solved numerically using a spectral element method (SEM2DPACK; Ampuero, 2009). I require at least five GLL nodes in the process zone to resolve the reduction from the static friction to dynamic friction during rupture propagation. To resolve ground motions at a maximum frequency of 6 Hz, I use a 75 m element mesh with five GLL nodes, so there are at least five nodes for the minimum wavelength in the simulations. The resolution test shows that in fact ground motions can be resolved to a maximum frequency of 7–8 Hz for the 75 m element. Thus, the results are shown up to a maximum frequency of 7 Hz. I allow frequency-independent seismic attenuation in the simulations by adding viscoelastic terms in the stress–strain relations (Moczo *et al.*, 2004). Three anelastic functions and relaxation frequencies are used to produce an approximately flat Q between 0.1 and 10 Hz. The details of the implementation of attenuation in dynamic rupture simulations are shown by Huang *et al.* (2014). For frequencies higher than 1 Hz, Q can be an increasing function of frequency and is modeled in the form of a power law (Withers *et al.*, 2015), though the frequency dependence of Q may affect ground motions on soil and rock sites in a similar fashion.

RESULTS

In this section, I present dynamic rupture scenarios and resulting ground accelerations for soil and rock simulations that have different velocity models and attenuation parameters. I discuss in more detail how the velocity models and attenuation parameters can change the variation of HVSRs and address why a depletion of high-frequency energy is observed on soil. I also show how rupture styles (buried vs. surface rupture), double-couple point sources, and velocity structure at shallow depth affect ground motions on soil and rock sites.

Dynamic rupture simulations

The values of fault friction and stresses in the simulations allow dynamic rupture to propagate at nearly the Rayleigh-wave-speed in both up-dip and down-dip directions shortly after nucleation (Fig. 2a,b). Different velocity models have a negligible effect on rupture speed, slip, and slip rate for depths larger than 3 km. The largest final slip is ~11 m near the hypocenter depth (10 km). If I define the along-dip rupture width as the region where slip is greater than 1% of the maximum final slip, then the rupture width is ~24 km in both models. Assuming that the rupture length is equal to the rupture width and slip at a given depth is the same along strike, simulated rupture generates earthquakes of magnitude ~7.3 for both model S and model R. The magnitude calculated from the 2D model is larger than the magnitude of a real earthquake with the same rupture area and peak slip, because the peak slip is assumed to extend along strike in the magnitude calculation.

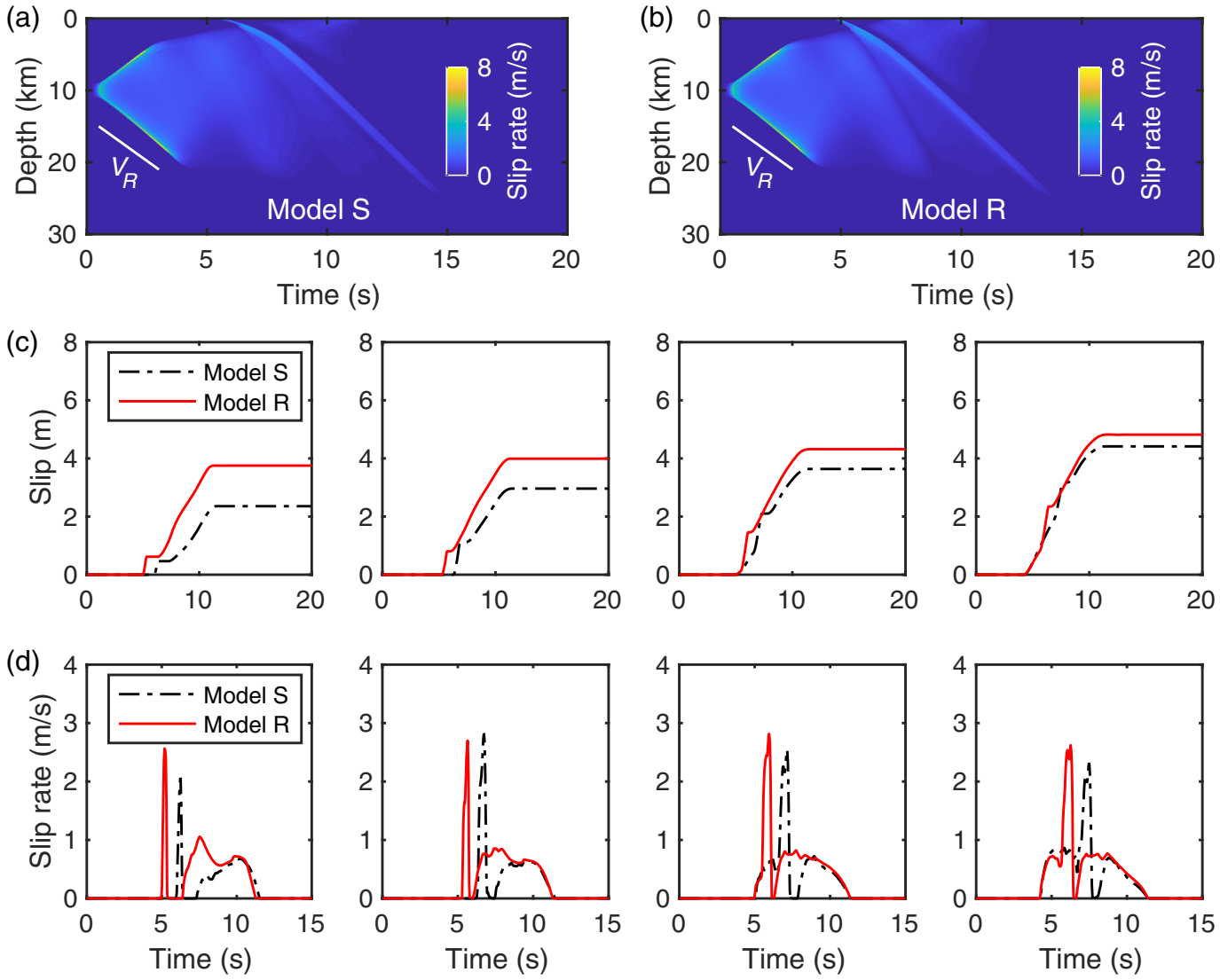

Figure 2. Comparison of (a,b) spatiotemporal distribution of slip rate, (c) slip, and (d) slip rate (low-pass filtered at 4 Hz) for model S and model R. V_R in panels (a) and (b) gives the Rayleigh-wavespeed and is equal to 0.92 V_S. Panels (c) and (d) show results at depths of 1, 2, 3, and 4 km from left to right. The color version of this figure is available only in the electronic edition.

At shallow depths, however, model S and model R exhibit different earthquake source properties. Rupture becomes significantly slower as it propagates through the shallow part of the fault for model S and results in smaller slip due to lower V_S. A detailed inspection of final slip shows that surface slip is only one-third of that for model R, and slip at 1 km depth is about two-thirds of that for model R. The difference in final slip gradually decreases with depth (Fig. 2c). Moreover, slip rate functions have multiple fluctuations and contain a mixture of sharp and smooth slip pulses for both models (Fig. 2d). The spatiotemporal slip rate distribution (Fig. 3a,b) reveals that the sharp slip pulse, a most noticeable feature in the slip rate function at shallow depths, originates from the surface *S*-wave reflection. Hence, sharp pulses appear earlier in slip rate functions of model R given its higher V_S at shallow depths. The smooth pulse following behind the sharp pulse has a larger average slip rate at shallow depths in model R, and rise time (i.e., the duration of slip rate function) is longer especially for depths shallower than 1 km. Together these two effects contribute to a larger shallow slip in model R.

Seismic acceleration waveform and spectra

The previous section shows that the lower V_S in model S results in smaller slip and slower rupture speed at the shallow part of the fault, but the overall characteristics of rupture propagation are very similar between the two models at depths larger 3 km, in which most seismic energy is radiated. Near-fault ground motions from these two rupture scenarios, however, exhibit distinct features, suggesting that different velocity models have a more significant influence on the propagation of seismic waves to near-fault stations. This important role of velocity models is further validated in the Buried Rupture Versus Surface Rupture section and Point-Source Models of

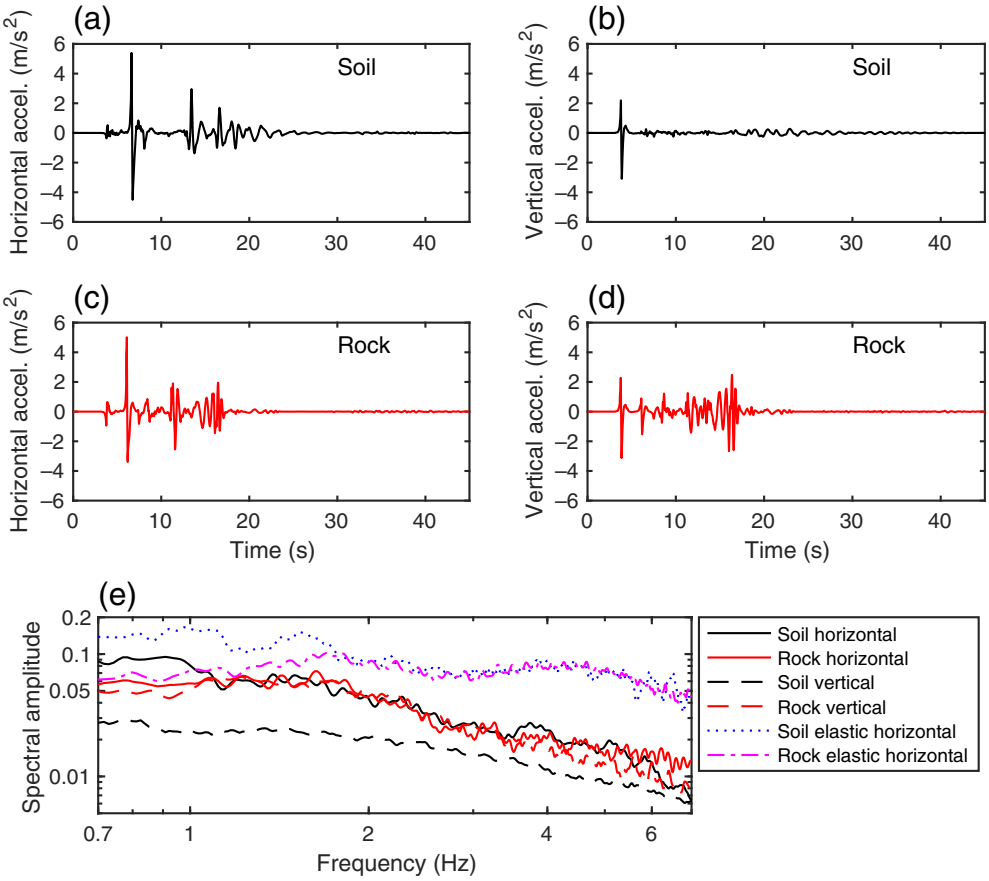

Figure 3. Plots of (a–d) simulated acceleration waveforms and (e) spectra for soil and rock sites at a distance of 10 km from the fault for surface rupture. The dotted and dashed-dotted lines show horizontal acceleration spectra for elastic soil and rock simulations, respectively. The color version of this figure is available only in the electronic edition.

Ground Motions on Soil and Rock Sites section for which rupture properties are either very similar throughout the fault or the same for different models. Figure 3 demonstrates ground acceleration recorded at a distance of 10 km from the fault. Both horizontal and vertical acceleration last for a longer duration on soil than on rock. Peak horizontal acceleration on soil is slightly larger than on rock, whereas peak vertical acceleration on soil is slightly lower. Vertical acceleration waveforms on soil and rock also have distinct characteristics. Vertical acceleration on soil stays at low amplitudes after the *P*-wave arrival, whereas vertical acceleration on rock has multiple large-amplitude peaks with the largest peak arriving at ~13 s after the *P*-wave arrival.

To understand the frequency dependence of near-field ground motions, I calculate acceleration spectra by taking a Fourier transform of the 45 s acceleration records (Fig. 3e). The spectra are smoothed using a 30-point moving average. For soil sites, I find spectral amplitudes of horizontal acceleration are considerably larger than those of vertical acceleration for the whole frequency band of interest (0.7–7 Hz). For rock sites, spectral amplitudes of horizontal acceleration are, on average, slightly larger than those of vertical acceleration at frequencies less than 1 Hz and higher than 4 Hz. Spectral amplitudes of horizontal and vertical components on rock become indistinguishable at 1–4 Hz.

Comparing horizontal acceleration spectra recorded by soil and rock sites, I find soil sites amplify near-field horizontal ground acceleration only at low frequencies. The horizontal spectral amplitude on soil is higher by about a factor of 1.7 at 0.7 Hz than on rock. At frequencies higher than 1.1 Hz, there is no significant difference between the soil and rock sites in horizontal spectral amplitudes, which agrees qualitatively with the finding by Joyner and Boore (1988). They suggested that similar horizontal high-frequency acceleration amplitudes for soil and rock sites can result from the suppression of high-frequency amplification by attenuation in the soil. However, my rupture simulations in a purely elastic medium, in which attenuation effects are not considered, still show similar horizontal acceleration amplitudes at higher frequencies for soil and rock sites (dotted and dashed-dotted lines in Fig. 3e).

HVSRs

I then calculate HVSRs for stations at distances of 5, 10, and 15 km on soil and rock sites (Fig. 4). To further investigate the effects of attenuation parameters, I also simulate ground motions from a rock model with the same attenuation parameters as the soil model (dashed lines in Fig. 4), that is, smaller Q_P and Q_S at shallow depths than the previous rock model. However, I find the difference between HVSRs on soil and rock sites has a weak dependence on attenuation parameters. Overall, HVSRs on soil are higher than those on rock at low frequencies. For the station at 5 km from the fault, HVSRs on soil approach those on rock at frequencies higher than 3 Hz. For the station at 10 km from the fault, HVSRs on soil become lower than those on rock at frequencies higher than 6 Hz. HVSRs on soil also share similar features at different stations:

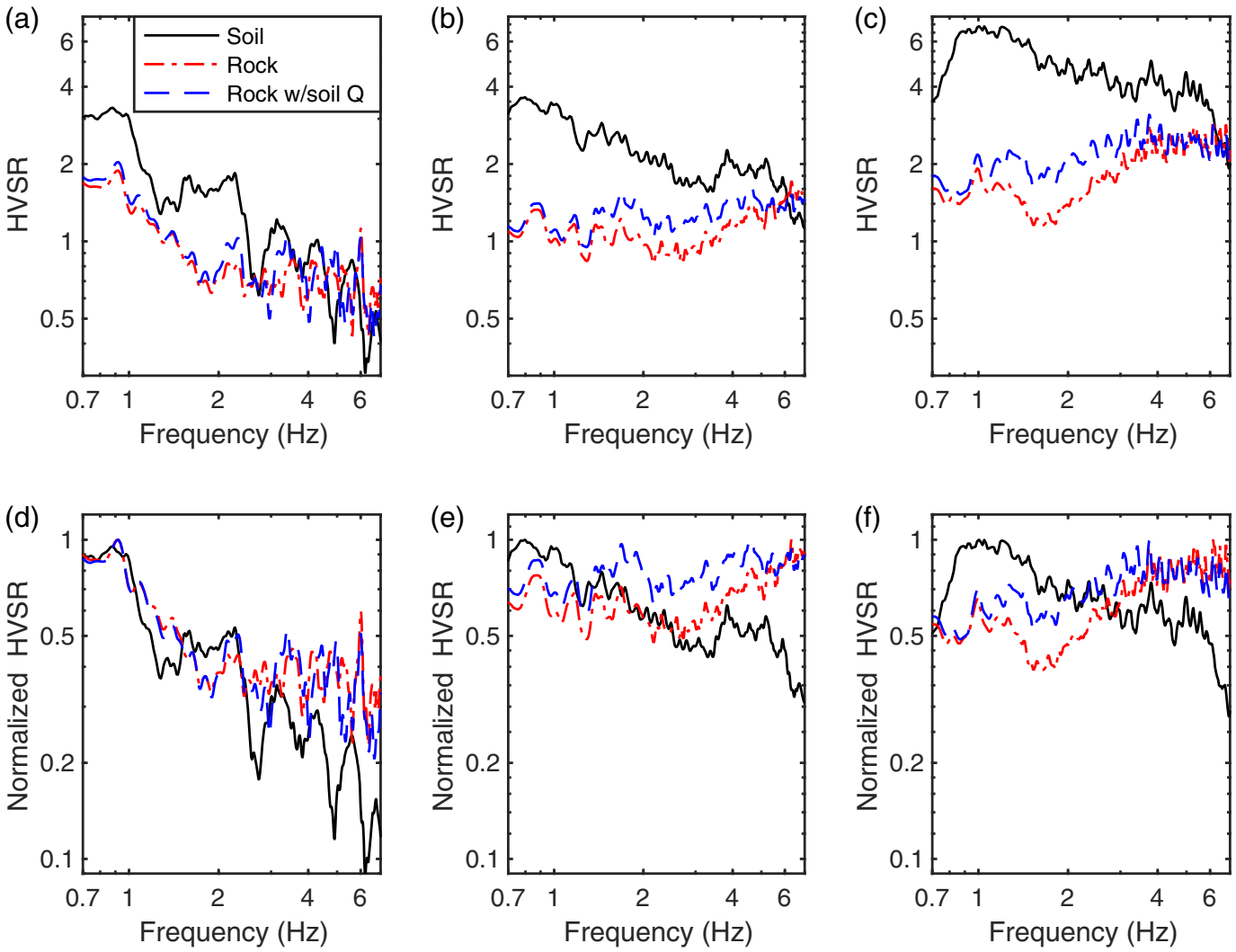

Their amplitudes are the largest at ~1 Hz and gradually decrease at higher frequencies. For the station at 10 km from the fault, HVSRs on soil are higher by a factor of ~3 at 1 Hz and by a factor of ~2 at 3 Hz than on rock.

To investigate the frequency dependence of HVSRs, I normalize them by the maximum amplitudes for the frequency band of interest. The normalized HVSRs clearly show that high-frequency content is relatively richer on rock than on soil (Fig. 4). This simulation result is qualitatively similar to the observed reduced amplitudes of high-frequency HVSRs at deep alluvium sites for the recent Ridgecrest earthquake (Hough *et al.*, 2020). It is worth noting that for the stations at 10 and 15 km distances, HVSRs on rock do not decay at high frequencies as observed in real data, but rather slightly increase in amplitudes. An even steeper increase in HVSRs at high frequencies may be observed in simulations if Q is modeled as an increasing function of frequency (Withers *et al.*, 2015). As discussed later, reproducing the exact behaviors of high-frequency HVSRs may require 3D rupture simulations or small-scale velocity heterogeneity that can generate more scattering of seismic waves.

Figure 4. Plots of (a–c) simulated horizontal-to-vertical spectral ratios (HVSRs) and (d–f) normalized HVSRs for soil and rock sites at distances of (a,d) 5, (b,e) 10, and (c,f) 15 km from the fault for surface rupture. The dashed-dotted lines show results from a rock simulation with different attenuation parameters from the soil simulation, whereas the dashed lines show results from a rock simulation with the same attenuation parameters as soil. The color version of this figure is available only in the electronic edition.

What causes the depletion of high-frequency energy on soil?

My analysis shows that low V_S and large Poisson's ratio of the shallow crust contribute to the amplification of low-frequency horizontal ground motions on soil, but it is intriguing why high-frequency horizontal ground motions are not similarly amplified as their low-frequency counterparts. The attenuation effect does not seem to play a role, as elastic simulations also produce similar horizontal acceleration amplitudes on soil and rock at higher frequencies (dotted and dashed-dotted lines in Fig. 3e). Besides the difference in V_S, the velocity models in my simulations have smooth velocity gradients, governed by the

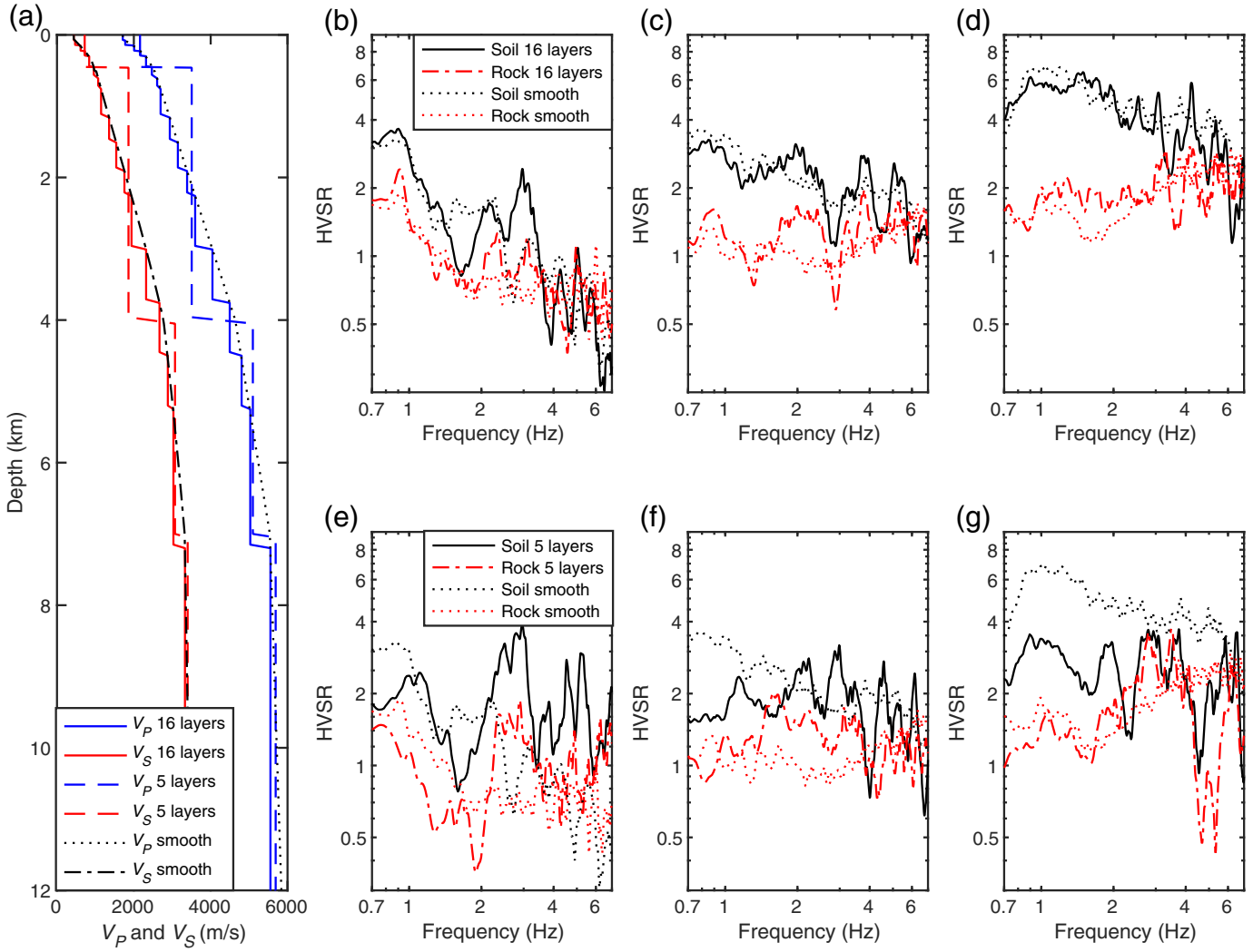

Figure 5. Illustrations of (a) the depth variation of seismic wave velocities underneath soil sites for the 16-layer velocity model (solid lines) and the 5-layer velocity model (dashed lines) compared with the smooth velocity gradient (dotted and dashed-dotted lines), as well as (b–g) simulated HVSRs for soil and rock sites at distances of (b,e) 5, (c,f) 10, and (d,g) 15 km from the fault for the 16-layer and 5-layer velocity models (solid and dashed-dotted lines) compared with the simulated HVSRs for soil and rock sites in smooth velocity models (dotted lines). The color version of this figure is available only in the electronic edition.

empirical relationships between seismic wave velocities and depths (Brocher, 2008). I hypothesize that a smooth velocity gradient may not be as efficient as a 1D layer model in amplifying high-frequency energy, because the velocity change within the wavelength that corresponds to a given high frequency would be small for a smooth velocity gradient.

To test this hypothesis, I generate two 1D layer models with seismic velocities directly derived from the smooth velocity gradient (Fig. 5). In the first model, I use 16 layers to closely mimic the smooth velocity gradient. In the second model, I define five velocity layers with the same boundaries (i.e., 0.5, 4, 7, and 12 km) used by Brocher (2008) to derive the empirical relationships. I then represent the seismic velocity for each layer using the median seismic velocity. The density and attenuation parameters are derived in the same way. I find that HVSRs on soil still decay at high frequencies for the 16-layer velocity model, and the contrasting behaviors of soil and rock sites are similar to the smooth velocity model. For the 5-layer velocity model, however, HVSRs on soil do not show a clear decay as frequency increases and have comparable amplitudes at low and high frequencies. The different outcomes of the 1D layer models suggest that a smooth velocity gradient or a velocity model with sufficient layers to mimic a smooth velocity gradient plays a critical role in the depletion of high-frequency energy on soil in my simulations.

Buried rupture versus surface rupture

Fault stress and frictional conditions in previous simulations allow rupture to reach the surface. Ground- motion observations suggest that surface rupture and buried rupture can have a strong influence on the characteristics of ground motions. For example, ground motions generated by surface rupture are weaker than

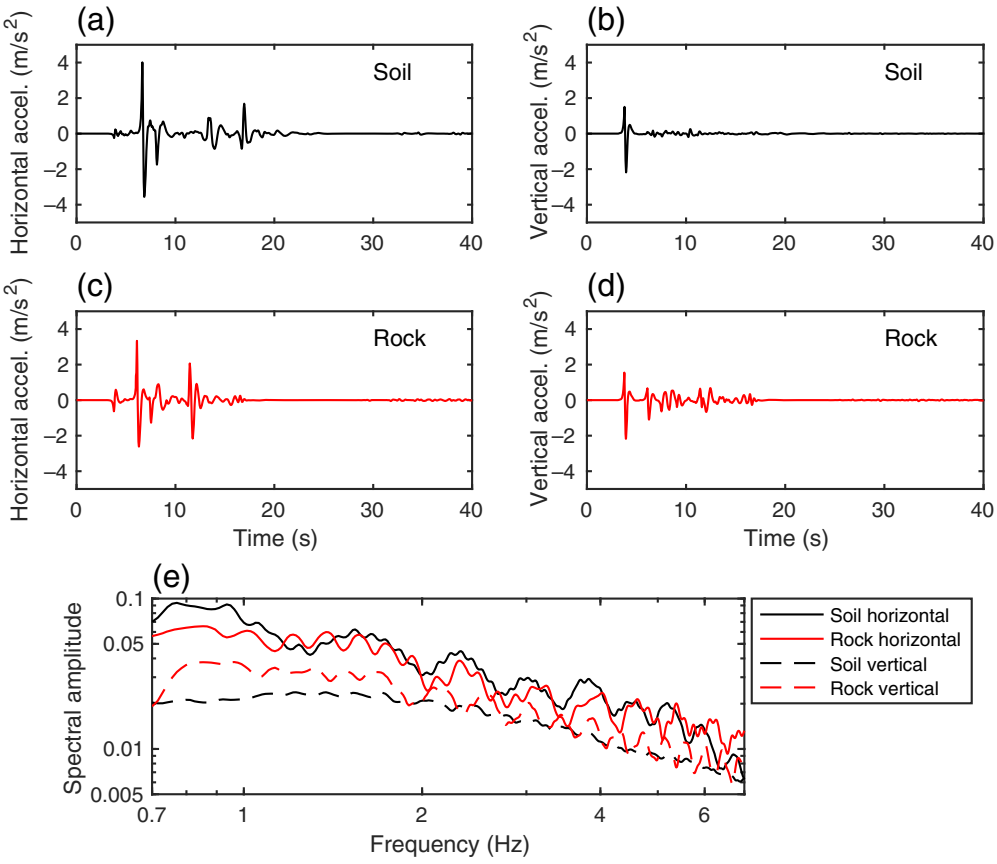

Figure 6. Plots of (a–d) simulated acceleration waveforms and (e) spectra for soil and rock sites at a distance of 10 km from the fault for buried rupture. The color version of this figure is available only in the electronic edition.

buried rupture for a period range of 0.3–3 s (Somerville, 2004). Such difference in ground motions can be attributed to a shallow weak zone as well as the larger stress drop and deeper hypocenter of buried rupture (Pitarka *et al.*, 2009). Here, I investigate how buried rupture influences the observed acceleration waveform and spectral features. The comparison between surface rupture and buried rupture also helps us understand how rupture propagation in the shallow crust affects the ground-motion difference between soil and rock sites.

To simulate buried rupture, I increase σ_0, μ_d, and D_c in the top 3 km to values that prevent rupture from reaching the surface for both velocity models. The buried rupture models have similar rupture properties at shallow depths. The resulting slip is less than 0.2 m for the top ~1 km and is zero near the surface. Magnitudes of simulated earthquakes are ~7.2, slightly smaller than the surface-rupturing scenarios. Near-source acceleration records of buried rupture show similar waveform features to surface rupture for the first 10 s after the *P*-wave arrival (Fig. 6), but wave reverberations afterward seem to be less pronounced on both soil and rock for buried rupture. On soil sites, because the lack of wave reverberations affects the apparent total duration of ground motions, spectral amplitudes of horizontal and vertical acceleration are slightly reduced at 0.7 Hz (Fig. 6). On rock sites, the lack of wave reverberations after the first 10 s has significantly reduced ground motions, especially for the vertical component. The peak vertical acceleration on rock arrives at 13 s after the *P*-wave arrival for surface rupture (Fig. 3). Compared to surface rupture, spectral amplitudes of vertical acceleration on rock are reduced by almost a half for buried rupture (Fig. 6). As a result, the HVSRs on rock are also larger for buried rupture (Fig. 7).

The larger HVSRs for buried rupture (Fig. 7), however, do not affect previous results regarding the difference of HVSRs on soil and rock. The results from buried rupture confirm the finding that different velocity models, rather than rupture processes, have a major influence on the contrasting behaviors of ground motions on soil and rock. For the station at 5 km distance, HVSRs on soil and rock are both increased by a factor of ~2 for buried rupture compared with the values for surface rupture at low frequencies. Thus, HVSRs on soil are still higher by a factor of 2–3 for frequencies around 0.7 Hz. For the station at 10 km distance, HVSRs on soil are higher by a factor of ~2 than on rock for frequencies around 1 Hz. Normalized HVSRs also support richer high-frequency energy on rock than on soil (Fig. 7). The contrast between normalized soil and rock HVSRs at 5 km distance is even larger for buried rupture than for surface rupture, especially for frequencies higher than 1.5 Hz.

Point-source models of ground motions on soil and rock sites

The dynamic rupture simulations have demonstrated that different velocity structures underneath soil and rock sites have a critical impact on high-frequency ground motions. Here, I show that the contrasts of HVSRs on soil and rock sites can also be observed in point-source models, in which the earthquake is represented by a double-couple source with a dip angle of 90° and a Gaussian source time function. The central frequency of the source time function is 1 Hz, which is near the corner frequencies of $M_w \sim 5$ earthquakes. The source

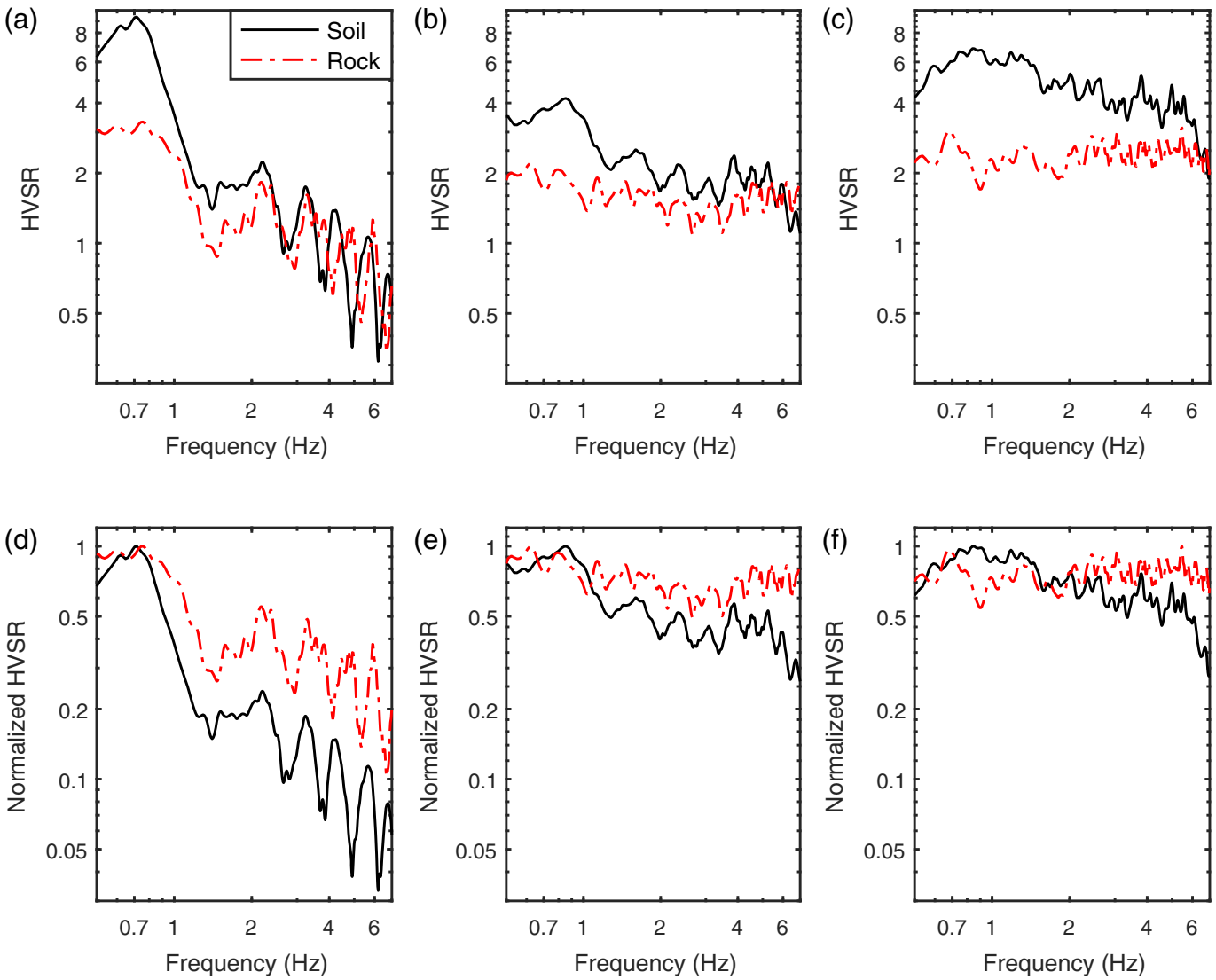

properties of earthquakes are the same for both soil and rock models.

Similar to dynamic rupture results, the simulated HVSRs on soil sites are significantly larger than those on rock sites at low frequencies (Fig. 8). The difference of HVSRs on rock and soil sites is especially large at 1–2 Hz for all the stations. HVSRs on soil gradually decay and approach those on rock at high frequencies. The normalized HVSRs also support richer high-frequency content in HVSRs on rock sites, though the HVSRs calculated from a point source appear to have a bump around 3 Hz for rock sites. Given the same earthquake source properties in point-source models, they demonstrate that the amplified low-frequency HVSRs and the rapid decay of HVSRs at high frequencies on soil sites are primarily the result of the smooth velocity structure.

Velocity models for the top 60 m

One remaining question in my dynamic rupture simulations is the effect of the velocity structure for the top 60 m. In previous simulations, seismic velocities are kept constant at this depth range to accurately calculate ground motions at a maximum frequency of 7 Hz with reasonable computational costs. In this section, I relax this model constraint and allow material properties to vary for the top 60 m. V_P and V_S are calculated from their depth variations for Holocene and Plio-Quaternary deposits at depths less than 60 m (Brocher, 2008). The density and attenuation parameters are also modified based on their relationships with seismic wave velocities. V_P, V_S, Q_P, and Q_S are 700 m/s, 215 m/s, 26, and 13 at surface, respectively, in the soil model. Thus, the soil site falls into site class D rather than site class C in the previous models. Figure 9a illustrates the differences of seismic wave velocities and density between

Figure 7. Plots of (a–c) simulated HVSRs and (d–f) normalized HVSRs for soil and rock sites at distances of (a,d) 5, (b,e) 10, and (c,f) 15 km from the fault for buried rupture. The color version of this figure is available only in the electronic edition.

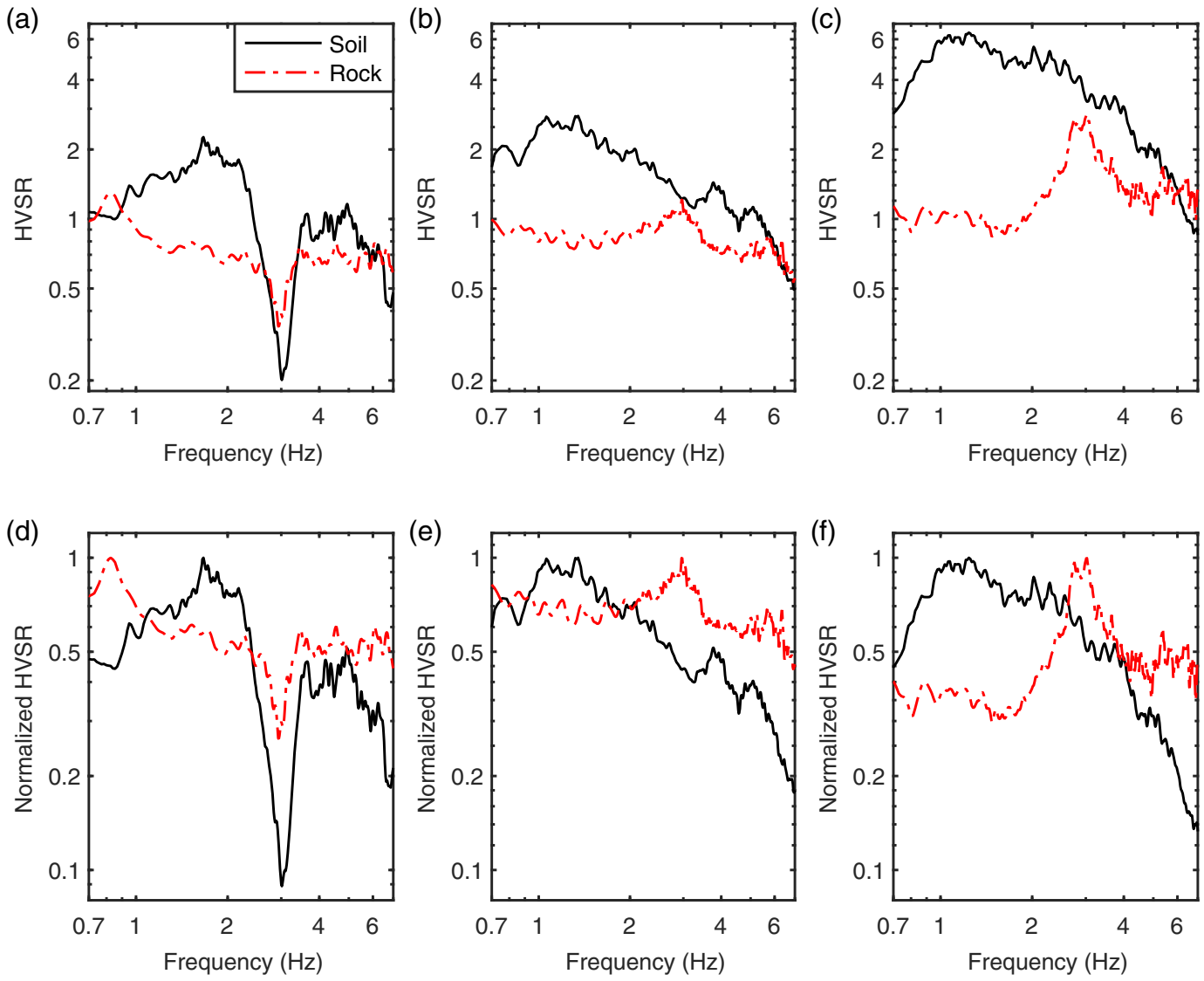

Figure 8. Plots of (a–c) simulated HVSRs and (d–f) normalized HVSRs for soil and rock sites at distances of (a,d) 5, (b,e) 10, and (c,f) 15 km from the fault for a double-couple source. The color version of this figure is available only in the electronic edition.

this velocity model and previous velocity model for soil sites. For a target maximum frequency of 3 Hz, there are at least five nodes for the minimum wavelength in the simulation.

The most noticeable feature of HVSRs resulting from this velocity model is an even faster decay of HVSRs on soil at high frequencies (Fig. 9). HVSRs on soil are generally higher than those on rock at frequencies lower than 1 Hz and decrease to values less than 1 at ~1, 2, and 3 Hz for stations at 5, 10, and 15 km distances, respectively. HVSRs on soil become lower than those on rock at frequencies higher than ~2.5 Hz. This interesting finding shows that the frequencies above which a depletion of high-frequency energy is observed in HVSRs also depend on the detailed velocity model at the shallowest depths.

DISCUSSION AND CONCLUSIONS

My dynamic rupture simulations unveil the important contribution of velocity structure to the observed difference in ground motions on soil and rock sites. The low V_S and large Poisson's ratios in the top 3 km of the crust underneath soil sites, in combination with a smooth velocity gradient, amplify horizontal ground motions at low frequencies but reduce vertical ground motions for the whole frequency range. As a result, HVSRs on soil tend to exhibit larger amplitudes than on rock at low frequencies, but HVSRs on soil decay more rapidly than those on rock at high frequencies in my simulations.

The simulated HVSRs are in qualitative agreement with the observed average HVSRs at deep alluvium sites for the recent Ridgecrest earthquake (Hough *et al.*, 2020). In the Ridgecrest observation, HVSRs at deep alluvium sites become lower than those on rock sites at frequencies above 3 Hz, which is observed in my simulations when material properties vary for the top

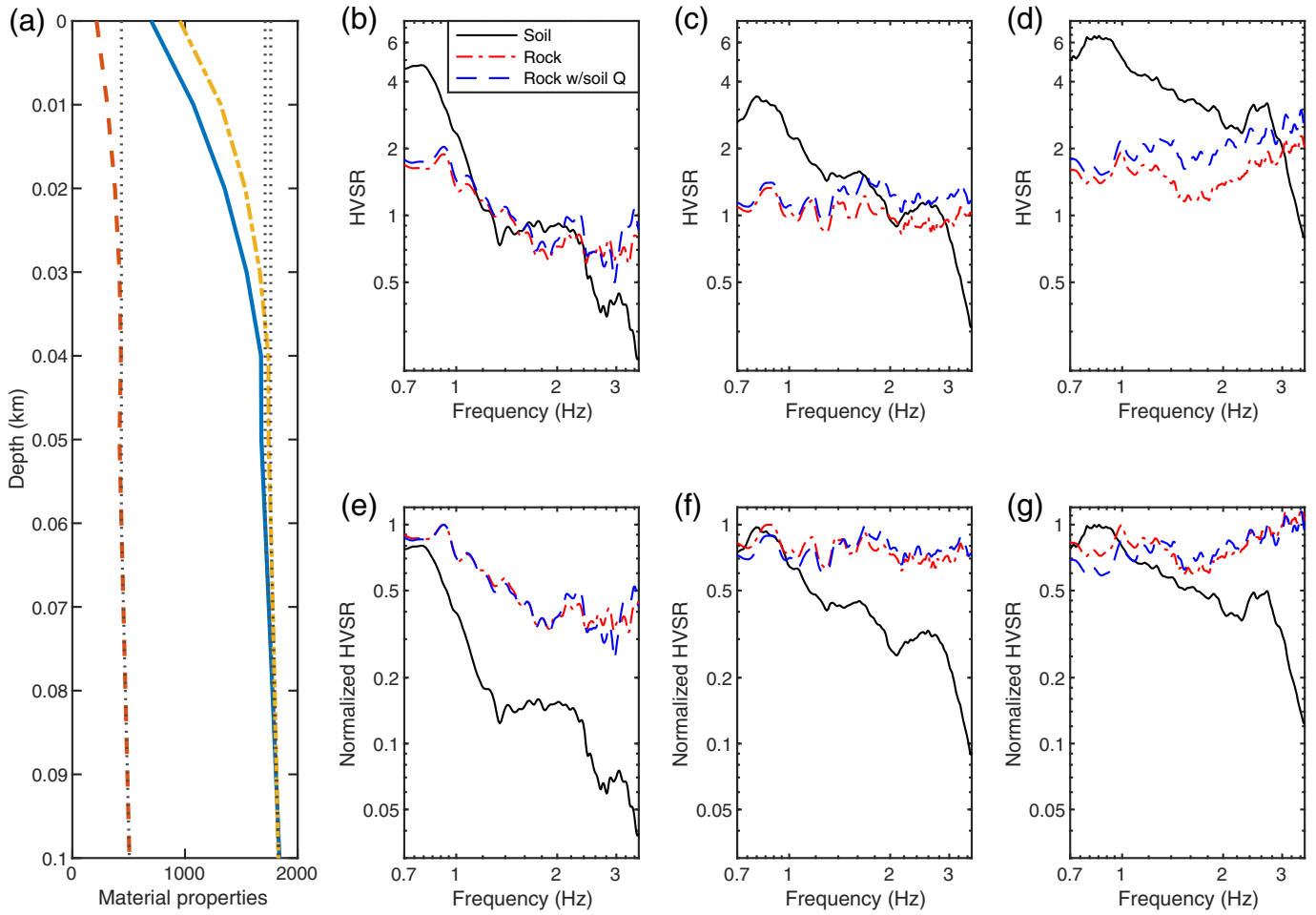

Figure 9. Illustrations of (a) the variation of V_P (solid line), V_S (dashed line), and density (dashed-dotted line) in the new soil velocity model for the top 100 m compared with the previous soil velocity model (dotted lines), as well as (b–d) simulated HVSRs and (e–g) normalized HVSRs for soil and rock sites at distances of (b,e) 5, (c,f) 10, and (d,g) 15 km from the fault. The color version of this figure is available only in the electronic edition.

60 m (Fig. 9), but not observed when V_S is kept constant at 460 m/s for the top 60 m. The better agreement between results from the velocity model with varying material properties for the top 60 m and the Ridgecrest observation may be related to the fact that they both assume site class D for soil sites. However, it should also be noted that my dynamic rupture simulations are not designed to fully capture the rupture characteristics of the Ridgecrest earthquake given its 2D nature. For example, the along-strike variation of rupture characteristics such as rupture directivity can modulate high-frequency ground motions. The exact behaviors of soil and rock sites can also be affected by the azimuths of stations in 3D simulations. Three-dimensional velocity models, especially those with the addition of small-scale material heterogeneity (Withers *et al.*, 2019), can cause strong scattering of wavefields and more variability in ground motions. Though the 2D rupture simulations may represent the contrasting behaviors of average HVSRs on soil and rock sites, future investigation should use a more realistic 3D dynamic rupture simulation with a full description of earthquake rupture and velocity model to reproduce the exact behaviors of observed HVSRs.

A key point that needs to be emphasized is that the smooth velocity model used in this study applies to the crustal scale (i.e., the upper ~15 km), which is fundamental for regional ground-motion simulations. However, the velocity structure for the top 100–200 m can also have a significant influence on high-frequency ground motions. It has been shown in 1D site-response models that overly coarse velocity profiles for the top 100–200 m generate large strain localizations above impedance contrasts between adjacent layers, which can cause more dissipation of high-frequency energy (Kaklamanos and Bradley, 2018; Kaklamanos *et al.*, 2020). This effect is contrary to the effect of a coarse crustal velocity model in my 2D dynamic rupture simulations (e.g., the 5-layer model in Fig. 5). The variability of velocity profiles at very shallow depths should also be accounted for in future dynamic rupture models that simulate high-frequency ground motions.

The results have great implications for the understanding of near-field ground motions. The diminished high-frequency energy in ground motions on soil sites is usually interpreted

as a result of nonlinear sediment response, which reduces high-frequency ground motions by increasing the damping of ground motions when shear strain increases (Beresnev and Wen, 1996). My dynamic rupture simulations demonstrate that a smooth crustal velocity model with low V_S underneath soil sites can cause different responses of horizontal and vertical ground motions and at least partially contribute to the depletion of high-frequency energy in the observed HVSRs. Some 3D ground-motion simulations have considered smooth velocity profiles based on a certain relationship between seismic wave velocities and depths (e.g., Harmsen *et al.*, 2008), and how high-frequency ground motions are influenced by smooth 3D velocity models in such simulations warrants further investigation. The results support the development of high-resolution velocity models at shallow depths and provide new physical constraints that can be used to better inform ground-motion simulations.

DATA AND RESOURCES

No data were used in this article. Dynamic rupture is solved using a modified version of SEM2DPACK (Ampuero, 2009).

DECLARATION OF COMPETING INTERESTS

The author acknowledges there are no conflicts of interest recorded.

ACKNOWLEDGMENTS

The author is grateful for the constructive comments provided by Ruth Harris, who suggested an important comparison with point-source models, and Steve Day, who pointed out the significant contribution of a smooth velocity gradient that forms the crux of the study. The author thanks Editor Jim Kaklamanos, Kyle Withers, and an anonymous reviewer for their constructive reviews. This article also benefits from the comments provided by Marlon Ramos, Jing Ci Neo, and Olivia Helprin. This study is supported by the National Science Foundation through Grant Award 1943742.

REFERENCES

Aagaard, B. T., R. W. Graves, A. Rodgers, T. M. Brocher, R. W. Simpson, D. Dreger, N. A. Petersson, S. C. Larsen, S. Ma, and R. C. Jachens (2010). Ground-Motion modeling of Hayward fault scenario earthquakes, part II: Simulation of long-period and broadband ground motions, *Bull. Seismol. Soc. Am.* **100,** 2945–2977.

Abercrombie, R. E. (1997). Near-Surface attenuation and site effects from comparison of surface and deep borehole recordings, *Bull. Seismol. Soc. Am.* **87,** 731–744.

Ampuero, J. P. (2009). SEM2DPACK: A spectral element method tool for 2D wave propagation and earthquake source dynamics, *User's Guide*, version 2.3.6, available at http://www.sourceforge.net/projects/sem2d/ (last accessed October 2019).

Andrews, D. J. (1976). Rupture propagation with finite stress in antiplane strain, *J. Geophys. Res.* **81,** 3575–3582.

Asano, K., H. Sekiguchi, T. Iwata, M. Yoshimi, T. Hayashida, H. Saomoto, and H. Horikawa (2016). Modelling of wave propagation and attenuation in the Osaka sedimentary basin, western Japan, during the 2013 Awaji Island earthquake, *Geophys. J. Int.* **204,** 1678–1694.

Beresnev, I. A., and K. L. Wen (1996). Nonlinear soil response—A reality? *Bull. Seismol. Soc. Am.* **86,** 1964–1978.

Bethmann, F., N. Deichmann, and P. M. Mai (2012). Seismic wave attenuation from borehole and surface records in the top 2.5 km beneath the city of Basel, Switzerland, *Geophys. J. Int.* **190,** 1257–1270.

Brocher, T. M. (2005). Empirical relations between elastic wavespeeds and density in the Earth's crust, *Bull. Seismol. Soc. Am.* **95,** 2081–2092.

Brocher, T. M. (2008). Compressional and shear-wave velocity versus depth relations for common rock types in northern California, *Bull. Seismol. Soc. Am.* **98,** 950–968.

Building Seismic Safety Council (BSSC) (2001). 2000 Edition, NEHRP Recommended Provisions for Seismic Regulations for New Buildings and Other Structures, FEMA-368, Part 1 (Provisions), Federal Emergency Management Agency, Washington, D.C.

Clayton, R., and B. Engquist (1977). Absorbing boundary conditions for acoustic and elastic wave equations, *Bull. Seismol. Soc. Am.* **67,** 1529–1540.

Dixit, A. M., A. T. Ringler, D. F. Sumy, E. S. Cochran, S. E. Hough, S. S. Martin, S. Gibbons, J. H. Luetgert, J. Galetzka, S. N. Shrestha, *et al.* (2015). Strong-Motion observations of the M 7.8 Gorkha, Nepal, earthquake sequence and development of the N-SHAKE strong-motion network, *Seismol. Res. Lett.* **86,** 1533–1539.

Edwards, B., and D. Fäh (2013). Measurements of stress parameter and site attenuation from recordings of moderate to large earthquakes in Europe and the Middle East, *Geophys. J. Int.* **194,** 1190–1202.

Esmaeilzadeh, A., D. Motazedian, and J. Hunter (2019). 3D nonlinear ground-motion simulation using a Physics-based method for the Kinburn basin, *Bull. Seismol. Soc. Am.* **109,** 1282–1311.

Field, E. H. (2000). A modified ground motion attenuation relationship for southern California the accounts for detailed site classification and a basin depth effect, *Bull. Seismol. Soc. Am.* **90,** S209–S221.

Field, E. H., P. A. Johnson, I. A. Beresnev, and Y. Zeng (1997). Nonlinear ground-motion amplification by sediments during the 1994 Northridge earthquake, *Nature* **390,** 599–602.

Frankel, A., W. Stephenson, and D. Carver (2009). Sedimentary basin effects in Seattle, Washington: Ground-Motion observations and 3D simulations, *Bull. Seismol. Soc. Am.* **99,** 1579–1611.

Graves, R. W., and A. Pitarka (2004). Broadband time history simulation using a hybrid approach, *13th World Conf. on Earthquake Engineering*, Vancouver, B.C., Canada, Paper No. 1098.

Harmsen, S., S. Hartzell, and P. Liu (2008). Simulated ground motion in Santa Clara Valley, California, and vicinity from M ≥ 6.7 scenario earthquakes, *Bull. Seismol. Soc. Am.* **98,** 1243–1271.

Harris, R. A., M. Barall, B. Aagaard, S. Ma, D. Roten, K. Olsen, B. Duan, D. Liu, B. Luo, K. Bai, *et al.* (2018). A suite of exercises for verifying dynamic earthquake rupture codes, *Seismol. Res. Lett.* **89,** 1146–1162.

Hauksson, E., and P. M. Shearer (2006). Attenuation models (QP and QS) in three dimensions of the southern California crust: Inferred fluid saturation at seismogenic depths, *J. Geophys. Res.* **111,** B05302, doi: 10.1029/2005JB003947.

Hough, S. E., E. Thompson, G. A. Parker, R. W. Graves, K. W. Hudnut, J. Patton, T. Dawson, T. Ladinsky, M. Oskin, K. Sirorattanakul, *et al.* (2020). Near-field ground motions from the July 2019 Ridgecrest, California, earthquake sequence, *Seismol. Res. Lett.* **91,** 1542–1555.

Huang, Y., J. P. Ampuero, and D. V. Helmberger (2014). Earthquake ruptures modulated by waves in damaged fault zones, *J. Geophys. Res.* **119,** 3133–3154.

Ida, Y. (1972). Cohesive force across the tip of a longitudinal-shear crack and Griffith's specific surface energy, *J. Geophys. Res.* **77,** 3796–3805.

Joyner, W. B., and D. M. Boore (1988). Measurement, characterization, and prediction of strong ground motion, *Earthquake Engineering and Soil Dynamics II, Proc. Am. Soc. Civil Eng. Geotech. Eng. Div. Specialty Conf.*, 27–30.

Kaklamanos, J., and B. A. Bradley (2018). Challenges in predicting seismic site response with 1D analyses: Conclusions from 114 KiK-net vertical seismometer arrays, *Bull. Seismol. Soc. Am.* **108,** 2816–2838.

Kaklamanos, J., B. A. Bradley, A. N. Moolacattu, and B. M. Picard (2020). Physical hypotheses for adjusting coarse profiles and improving 1D site-response estimation assessed at 10 KiK-net sites, *Bull. Seismol. Soc. Am.* **110,** 1338–1358.

Kubo, H., T. Nakamura, W. Suzuki, Y. P. Dhakal, T. Kimura, T. Kunugi, N. Takahashi, and S. Aoi (2019). Ground-motion characteristics and nonlinear soil response observed by DONET1 seafloor observation network during the 2016 southeast off-Mie, Japan, *Bull. Seismol. Soc. Am.* **109,** 976–986.

Ludwig, W. J. (1970). Seismic refraction, *The Sea* **4,** 53–84.

Meza-Fajardo, K. C., J. F. Semblat, S. Chaillat, and L. Lenti (2016). Seismic-wave amplification in 3D alluvial basins: 3D/1D amplification ratios from fast multipole BEM simulations, *Bull. Seismol. Soc. Am.* **106,** 1267–1281.

Moczo, P., J. Kristek, and L. Halada (2004). *The Finite-Difference Method for Seismologists: An Introduction*, Comenius University, Bratislava.

Neighbors, C., E. J. Liao, E. S. Cochran, G. J. Funning, A. I. Chung, J. F. Lawrence, C. Christensen, M. Miller, A. Belmonte, and H. H. A. Sepulveda (2015). Investigation of the high-frequency attenuation parameter, κ (kappa), from aftershocks of the 2010 M w 8.8 Maule, Chile earthquake, *Geophys. J. Int.* **200,** 200–215.

Nicholson, C., and D. W. Simpson (1985). Changes in Vp/Vs with depth: Implications for appropriate velocity models, improved earthquake locations, and material properties of the upper crust, *Bull. Seismol. Soc. Am.* **75,** 1105–1123.

Olsen, K. B. (2000). Site amplification in the Los Angeles basin from three-dimensional modeling of ground motion, *Bull. Seismol. Soc. Am.* **90,** S77–S94.

Park, S., and S. Elrick (1998). Predictions of shear-wave velocities in southern California using surface geology, *Bull. Seismol. Soc. Am.* **88,** 677–685.

Pitarka, A., L. A. Dalguer, S. M. Day, P. G. Somerville, and K. Dan (2009). Numerical study of ground-motion differences between buried-rupturing and surface-rupturing earthquakes, *Bull. Seismol. Soc. Am.* **99,** 1521–1537.

Pitarka, A., R. Gok, G. Yetirmishli, S. Ismayilova, and R. Mellors (2016). Ground motion modeling in the eastern Caucasus, *Pure Appl. Geophys.* **173,** 2791–2801.

Rodgers, A. J., A. Pitarka, R. Pankajakshan, B. Sjögreen, and N. A. Petersson (2020). Regional-Scale 3D ground-motion simulations of Mw 7 earthquakes on the Hayward fault, northern California resolving frequencies 0–10 Hz and including site-response corrections, *Bull. Seismol. Soc. Am* **110,** 2862–2881.

Rodgers, A. J., A. Pitarka, N. A. Petersson, B. Sjögreen, and D. B. McCallen (2018). Broadband (0–4 Hz) ground motions for a magnitude 7.0 Hayward fault earthquake with three-dimensional structure and topography, *Geophys. Res. Lett.* **45,** 739–747.

Somerville, P. (2004). Differences in earthquake source and strong ground motion characteristics between shallow and buried faulting, *Proc. of OECD/NEA Workshop*, 5 pp.

Taborda, R., and J. Bielak (2014). Ground-motion simulation and validation of the 2008 Chino Hills, California, earthquake using different velocity models, *Bull. Seismol. Soc. Am* **104,** 1876–1898.

Trifunac, M. D., and M. I. Todorovska (1998). Nonlinear soil response as a natural passive isolation mechanism—the 1994 Northridge, California, earthquake, *Soil Dynam. Earthq. Eng.* **17,** no. 1, 41–51.

Van Houtte, C., S. Drouet, and F. Cotton (2011). Analysis of the origins of κ (kappa) to compute hard rock to rock adjustment factors for GMPEs, *Bull. Seismol. Soc. Am* **101,** 2926–2941.

Wang, Y., S. M. Day, and M. A. Denolle (2019). Geometric controls on pulse-like rupture in a dynamic model of the 2015 Gorkha earthquake, *J. Geophys. Res.* **124,** 1544–1568.

Wang, Y. J., K. F. Ma, S. K. Wu, H. J. Hsu, and W. C. Hsiao (2016). Near-Surface attenuation and velocity structures in Taiwan from wellhead and borehole recordings comparisons, *TAO* **27,** 169–180.

Wills, C., M. Petersen, W. Bryant, M. Reichle, G. Saucedo, S. Tan, G. Taylor, and J. Treiman (2000). A site-condition map for California based on geology and shear-wave velocity, *Bull. Seismol. Soc. Am.* **90,** S187–S208.

Withers, K. B., K. B. Olsen, and S. M. Day (2015). Memory-Efficient simulation of frequency-dependent Q, *Bull. Seismol. Soc. Am.* **105,** 3129–3142.

Withers, K. B., K. B. Olsen, S. M. Day, and Z. Shi (2019). Ground motion and intraevent variability from 3D deterministic broadband (0–7.5 Hz) simulations along a nonplanar strike-slip fault ground motion and intraevent variability from 3D deterministic broadband simulations, *Bull. Seismol. Soc. Am.* **109,** 229–250.

Manuscript received 12 October 2020
Published online 15 June 2021